

The characteristics of the recirculating bulge region in coastal buoyant outflows

by Greg Avicola^{1,2} and Pablo Huq¹

ABSTRACT

A relatively large recirculating gyre, or bulge (anticyclonic buoyant lens) region attached to the source has been observed to occur in some numerical simulations and in some oceanic outflows. The purpose of this paper is to determine the dynamics of such recirculating bulge regions. Laboratory experiments were conducted for the purpose of examining the characteristics, evolution, and impact of a recirculating bulge in a coastal buoyant outflow. All experiments were performed such that the buoyant layer was thin compared to the total water depth, and the width of the bay exit was approximately equal to the internal Rossby deformation radius of the buoyant outflow. The geometry of the bay-exit (radius of curvature and exit angle) was varied in order to produce experiments with recirculating bulge formation, and experiments without. Measurements of the density and velocity fields were undertaken. The dimensions of the recirculating bulge were found to evolve identically (when appropriately scaled) for all experiments in which such a bulge formed, regardless of bay-exit geometry. When recirculating bulges formed, it was determined that the freshwater storage within the bulge was approximately 60–70% of the source freshwater flux. The impact on the attached coastal current downshelf of the recirculating bulge was found to be significant: the width, length, and velocities of such attached coastal currents were much reduced in comparison to coastal currents that evolved in the absence of a recirculating bulge. Growth rates of the bulge were measured with time: the recirculating bulge was found to grow radially as $\sim t^{2/5}$ and vertically as $\sim t^{1/5}$. Baroclinic instabilities were observed in the recirculating bulge. The instabilities evolved as multiple rotating cores within the larger anticyclonic gyre. The presence of the instabilities in the recirculating bulge may account for its relatively large radial growth but weak vertical growth.

1. Introduction

Buoyant fluid entering the coastal ocean through a strait or estuary will often form a buoyancy-driven coastal current. Such currents are common and can stretch for hundreds of kilometers along the coastline. Examples of observed coastal currents include the Columbia River Plume (e.g., Hickey *et al.*, 1998), the Rhine Outflow (e.g. Simpson *et al.*, 1993), and the Delaware Coastal Current (e.g. Münchow and Garvine, 1993a,b). Past studies have also found that in addition to the coastal current, a larger (in across-shelf extent) feature may form a recirculating gyre or bulge at the buoyant source exit (e.g.

1. College of Marine Studies, University of Delaware, Newark, Delaware, 19716, U.S.A. *email*: huq@udel.edu

2. Present address: College of Oceanic and Atmospheric Sciences, Oregon State University, Corvallis, Oregon, 97331, U.S.A.

Kawasaki and Sugimoto, 1984). Such bulge regions act as intermediate connections between a coastal current and its associated freshwater source. Studies have been partially motivated by field observations in which a recirculating bulge may be present; however, the limited spatial density of many observational studies, combined with the fact that most such studies are not synoptic, leaves open questions regarding the details of the bulge dynamics and of how ubiquitous recirculating bulges are in nature.

One such gyre/coastal current system seen in nature is formed from the exchange flow between the Pacific Ocean and the Sea of Japan at the Tsugaru Strait. Kawasaki and Sugimoto (1984) investigated seasonal variations in the behavior of the buoyant outflow (produced from thermal differences). Between January and June, the Tsugaru warm current was observed to form directly at the exit of the strait. However, during the months of July through December, a large anticyclonic gyre formed at the mouth instead.

A second example of such a system observed in nature occurs in the Alboran Sea: relatively fresh Atlantic water flows through the Strait of Gibraltar to form a recirculating gyre and coastal current. Studies first identified the gyre through observations of sea surface dynamic height (Lanoix, 1974). Subsequently, laboratory studies were conducted to examine the gyre by Whitehead and Miller (1979), Bormans and Garrett (1989), and Klinger (1994a,b).

Process studies were conducted to investigate this problem, with the goal of understanding the formation mechanisms of the gyre. Bormans and Garrett (1989) studied the role of the curvature of the bay exit in laboratory experiments. They observed that their experiments produced either a jet (coastal current) or gyre (recirculating bulge) depending upon the radius of curvature of the bay exit. Klinger (1994b) examined the formation of eddies from a sharp corner in laboratory experiments: he observed that eddies were generated at corner angles of greater than 45 degrees. In numerical modeling studies, it was found that such recirculating bulge features are often present in the simulations. For example, in the study of Oey and Mellor (1993) a strong recirculating bulge region is evident. Fong (1998) evaluated the growth rates of the recirculating bulge in his numerical study and examined the effect of the bulge on the magnitude of the transport of the downshelf coastal current. Nof and Pichevin (2001) presented a theory that predicts recirculating bulge growth and suggested that such a feature must occur in order to balance the alongshore momentum flux of the coastal current. They predict the growth rates of the recirculating bulge analytically and compare the results to numerical simulations.

The purpose of this study is to examine the growth of such recirculating bulge regions, and to examine their impact on the surrounding coastal ocean. After formation, the recirculating bulge region grows; buoyancy is 'stored' in the bulge, the net inflow from the source exceeds the outflow into the coastal current. Thus, the freshwater flux entering the downshelf coastal current is reduced if a recirculating bulge forms, as some fraction of the source freshwater flux is stored in the growing recirculating bulge. Therefore, the magnitude of the volume flux stored in the recirculating bulge is an important question, as it has a large influence on the physical extent and velocity and scales of the downshelf



coastal current transport. Similarly, the physical extent of the recirculating bulge region is an important question. The buoyant fluid exiting the bay or strait will have a significant density difference (due to temperature, salinity, or both) from the ambient coastal ocean. Furthermore, any biological material or pollutants present in the discharge from the source bay or strait will be stored within this large freshwater feature.

In a companion paper to this study (Avicola and Huq, 2003), the formation of a recirculating bulge is examined in laboratory experiments. In that study, the role of the bay exit geometry on the formation of a recirculating bulge is examined. It was found that recirculating bulge formation was governed both by the geometry of the exit and the scales of the outflow, and that a recirculating bulge was observed to form based on the value of the impact angle, Φ , of the exiting fluid. This paper will not delve into the mechanics of how bulge formation is dependent upon coastal geometry. Instead, we will simply refer to experiments in which bulge formation was present, and those in which it was not. Table 1 lists the experiments performed with values for the relevant parameters. The experiments in which a recirculating bulge formed are marked with light gray shading.

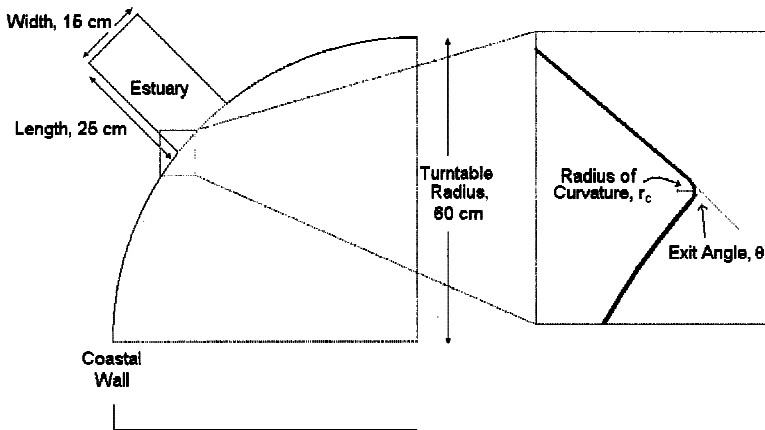


Figure 1. Schematic in which the tank used to conduct the experiments of this study is portrayed. A quarter-section of the tank is shown above in plan view, below is shown a cross-sectional view of the bathymetry. The tank has an estuary set into its sidewall with a width of 15 cm and length of 25 cm. The estuary bottom is flat, and is set flush against the bottom of the coastline. The depth of the estuary (and the depth of the fluid along the coastal wall) is controlled in an experiment by controlling the total volume of water used in the experiment. Plexiglas inserts are available that can be placed within the estuary to change the dimensions of the estuary. The insets were used to control the estuary width, the exit angle, and the radius of curvature (shown to the right as an inset box). For the experiments conducted, the width was set so that the bay exit Kelvin number was order 1.

conducted for a bay Kelvin number (defined as the ratio of the estuary width to the internal Rossby radius of the flow) of order 1 (Garvine, 1995). Additionally, all experiments were conducted for an ambient depth parameter (defined as the ratio of the scale depth of the plume to the relative water depth) of order 0.1 (Yankovsky and Chapman, 1997; Avicola and Huq, 2002). Thus, in the experiments conducted, the freshwater outflow (~ 2 cm deep) is isolated from the bottom by a deep, relatively inactive, layer of ambient ocean water (~ 10 cm deep).

The bay was constructed in such a manner that insets could be placed within it to alter the geometry. For the experiments conducted, insets were used that varied the outlet angle or the radius of curvature of the bay: such variations in the exit parameters resulted in flows with and without recirculating bulge formation, as tabulated in Table 1. The details of the role of the exit angle and radius of curvature are discussed in a companion paper (Avicola and Huq, 2003): this study will examine the differences between experiments with and without recirculating bulge formation.

The tank was filled with ambient ocean water of a specified salinity. Freshwater was used as a source for the buoyant outflow, held in a smaller co-rotating tank. The freshwater source was a pipe, with a radius of 1 cm, set into the rear of the bay. The freshwater was driven by gravity through a calibrated flow meter at a specified flow rate. A specified

rotation rate was set before each experiment. The ambient ocean fluid was allowed to reach solid body rotation before each experiment was begun. The table was rotated in the counter-clockwise direction, which corresponds to the northern hemisphere's sense of rotation (f is positive). For these experiments, the turntable was leveled to an accuracy of 0.001 radians. This accuracy, combined with the large total water depth, eliminated artificial tidal motions within the experiment's measurement capability. Rotation period was measured to an accuracy of $\Delta T = 0.01$ seconds, which translates to an error of 0.002–0.0001 rad/s, depending on the experiment. The parabolic free surface induced by the rotating tank is dynamically insignificant: the tank itself is an order of magnitude smaller than the scale necessary for the induced topographic beta effect to be a first order forcing. A Plexiglas cover was fitted over the turntable, in order to eliminate surface wind-stress and evaporative cooling.

Data in the experiments were collected visually through overhead video observations. A Sony 450 \times digital video camcorder was suspended above the tank, providing video records in the frame of reference of the turntable. The buoyant outflow fluid was marked using small concentrations of Rhodamine dye. This dye served as a clear visual indicator of the location of freshwater within the tank. Additionally, the flow was seeded with reflective surface drifters, typically 0.5 mm in size. These drifters were tracked in space and time from the video records to provide information on recirculating bulge/coastal current dimensions and velocities. Images of experimental runs are presented which were captured from video. These images have been enhanced in Adobe Photoshop; an artificial gradient mapping was used to accentuate the differences in color gradients within the image, which clarifies the still images considerably.

Additionally, in some experiments, measurements were taken to determine the density field. Hypodermic probes of 0.8 mm diameter were located at specific points in the flow in order to obtain density cross-sections measured using an optical refractometer.

For this study, density cross-sections in the offshore direction (y - z plane) were taken. The cross-sections were taken at one downshelf location ($x = 50$ cm) by measuring density samples at various points in the y - z plane. At each point, density samples were taken to establish the mean density for the point. Six probes were operated simultaneously during a single experiment; therefore, a number of experiments were undertaken to complete an entire cross-section. Cross-sections were constructed from the data of a number of horizontal transects. In some locations, overlapping vertical transects were added to establish vertical density gradients accurately. Variability existed in density measurements at a point within a single experiment: variability at a point within multiple experiments was of the same magnitude. Density measurements were accurate to within 5% or better.

Dimensional measurements (lengths, times, etc.) will be presented in nondimensional form in order to compare results directly between experiments and between studies and observations. The volume transport of a two-layer frontal structure in thermal wind balance can be expressed as:

$$Q_g = \frac{z^2 g'}{2f} \quad (1)$$

where Q_g is the geostrophic transport, z is the maximum depth of the front, g' is the local reduced gravity of the front, and f is the local Coriolis parameter. A scale depth can be produced from Eq. 1 by scaling Q_g and g' by the source values Q_0 and g'_0 . This scale depth, h , is:

$$h = \sqrt{\frac{2Q_0 f}{g'_0}}. \quad (2)$$

Based upon this scale depth estimate, a horizontal length scale, R , and a velocity scale, c , can be written as:

$$R = \frac{\sqrt{g'_0 h}}{f}. \quad (3)$$

$$c = \sqrt{g'_0 h} \quad (4)$$

Elapsed time is nondimensionalized by the rotation period of the rotating system, T . For a rotating turntable, T is simply $4\pi/f$, or $4\pi R/c$. While the geostrophic scales h , R , and c are most applicable to a coastal current system (they are derived based upon scaling the transport in a semi-geostrophic two layer frontal structure) it will be shown that they also scale the evolution and characteristics of the recirculating bulge region.

3. Characteristics of the recirculating bulge

The objective of this paper is to examine the growth and characteristics of a recirculating bulge and its impact on the downshelf coastal current. Data will be presented that quantifies the effect of the recirculating bulge on the coastal current. Data of the evolution of the bulge's width, length, and depth as a function of time will also be shown. From such information, volume- flux and density anomaly- flux estimates into and out of the bulge can be estimated, and the impact of the bulge can be ascertained.

Figure 2 is a schematic which portrays the evolution of a buoyant outflow exiting a 90-degree, $K = 1$ estuary (90-degree refers to the angle between the buoyant outflow and the coastal wall). The schematics are representative of the observed experimental outflows for such experiments. As the initial outflow exits the bay, the velocity vector is oriented primarily in the across-shore direction as the buoyant outflow moves offshore (across-shelf). This is the situation portrayed in the upper panel of Figure 2. However, the Coriolis force begins to turn the buoyant intrusion to the right (northern hemisphere): at a time of approximately $1/4$ rotation period. Subsequently, the buoyant outflow doubles back upon itself and is observed to impact the coastal wall. The angle formed between the impact velocity vector and the coastal wall is defined as the impact angle, Φ . As shown in the companion paper (Avicola and Huq, 2003), for a sufficiently large impact angle, a

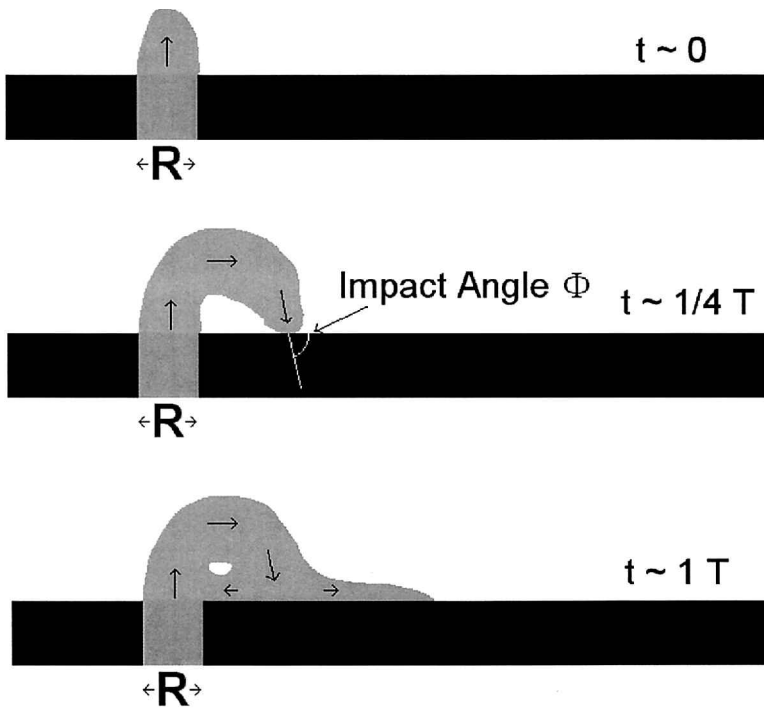


Figure 2. Schematic showing the early times of the flow which lead to the formation of a recirculating bulge. Time $t = 0$ is defined as the moment at which the buoyant fluid exits the bay (here shown as a $K = 1$ bay, for which the width is equal to the Rossby radius). If the bay exit is such that the buoyant fluid separates from the coastal wall as it exits the bay, it will form an offshore 'tongue' or intrusion. The upper panel is a snapshot of this situation, in which the buoyant fluid is seen moments after it has exited the bay region. After approximately $1/4$ of a rotation period, T , the buoyant fluid has made an inertial turn, and impacts the coastal wall some distance downshelf of the bay exit, at an impact angle, Φ . For values of the impact angle larger than 60-degrees, a recirculating bulge was observed to form, as sufficient fluid is transported upshelf from the impact point, forming a recirculating gyre. The lower panel depicts this situation, in which the buoyant outflow has formed a nascent bulge, as well as the start of a coastal current.

recirculating bulge forms in addition to the downshelf coastal current: recirculating bulge formation was observed to occur for impact angles greater than 60°. The lower panel of Figure 2 portrays this nascent bulge — coastal current system at a time of one rotation period after the start of the experiment.

a. Growth estimates of the recirculating bulge

The values of the parameters of the experiments conducted for this study are listed in Table 1; four of the experiments had sufficiently large values of the impact angle to form a recirculating bulge. The overall dimensions of the recirculating bulge were estimated from

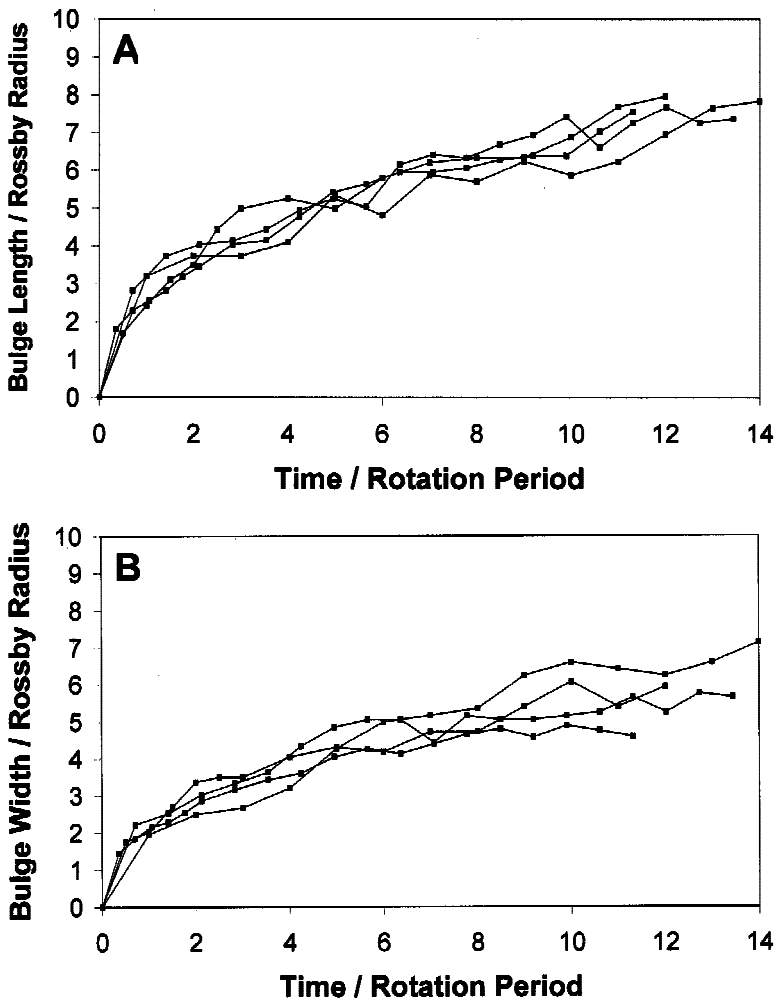


Figure 3. Graphs of recirculating bulge scales as a function of time. Panel A is a plot of the bulge length (along-shelf extent), Panel B is a plot of the bulge width (across-shelf extent), and Panel C is a plot of the bulge depth. All plots are shown in nondimensional form.

video records of the flow field. In describing the physical dimensions of the bulge region, the following conventions will be used: 'length' will be used to denote the along-shelf maximum extent (or along-shelf diameter), 'width' will be used to denote the across-shelf maximum extent (or across-shelf diameter), and depth will be used to denote the maximum depth.

Figure 3 is composed of three graphs of recirculating bulge evolution: Panel A is a plot of bulge length, Panel B is a plot of bulge width, while Panel C is a plot of bulge depth, all evolving as a function of time. The graphs have been nondimensionalized by the scales

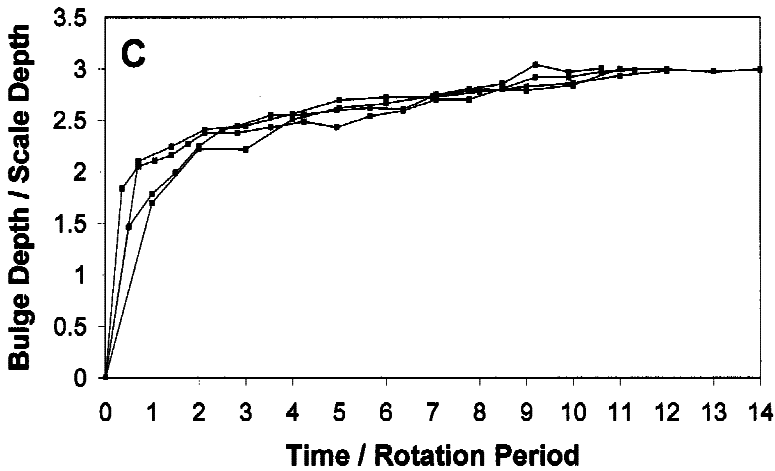


Figure 3. (Continued)

outlined in Section 2. A value of time equal to zero corresponds to the time at which the buoyant fluid exited the bay. The data presented in Panels A and B demonstrate that the recirculating bulge is a large feature (in the horizontal) that grows quickly in time. After 14 days of growth ($t/T \sim 14$) the recirculating bulge is $\sim 7R$ in diameter: in comparison, the downshelf coastal current is typically $\sim 2R$ in extent at the same timeframe (Avicola and Huq, 2002). Values of the recirculating bulge length are found to be greater than the width, on average; the corresponding ellipticity is approximately 1.3 and is constant with time. The bulge depth increases slightly over the same time frame, from $2h$ to $3h$ in depth over 14 days of evolution.

b. Estimates of coastal current transport

The impact of the recirculating bulge on the coastal current can be observed indirectly by examining the evolution of the coastal current. Figure 4 is a set of four graphs of the evolution of the downshelf coastal current. Figures 4A and 4C show current downshelf distance as a function of time; whereas, Figures 4B and 4D show width as a function of time. Figures 4A and 4B present data in which the bay exit angle has been varied, while Figures 4C and 4D present data in which the radius of curvature has been varied. In all four panels, the experiments are observed to fall into one of two groupings. The upper grouping of experimental data on each graph contains data from experiments in which a recirculating bulge did not form. In Panels A and C, experiments which did not possess bulges formed longer coastal currents (with correspondingly larger velocities). Panels B and D show that such bulge-less experiments formed wider coastal currents. Conversely, the lower grouping of experimental data on each graph shows data from experiments for which a recirculating bulge was observed to form. Note that in all the data shown, the impact of the

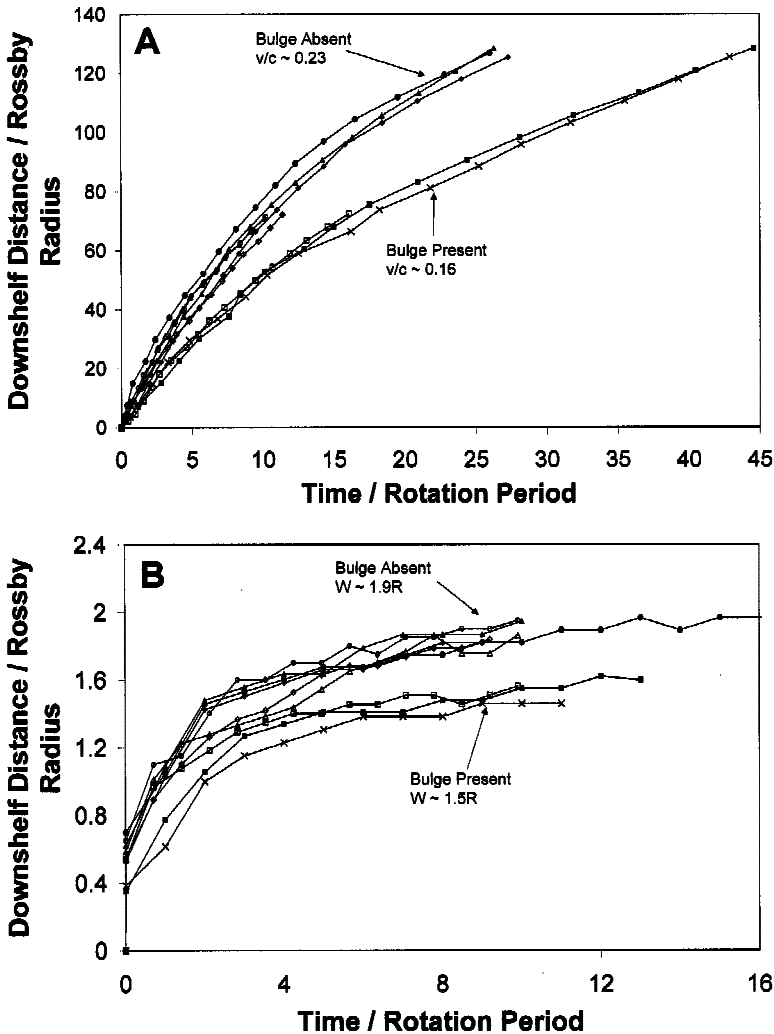


Figure 4. Graphs in which coastal current evolution data are plotted against time. Panels A and C are graphs of coastal current nose position, while Panels B and D are graphs of coastal current width. Data are nondimensionalized by the internal Rossby Radius, R , and the rotation period, T . Panels A and B show data for experiments in which the bay exit angle has been varied. Panels C and D show data for experiments in which the bay radius of curvature has been varied. Note that in all four panels, there are two distinct groupings. The upper grouping is composed of experiments in which a recirculating bulge did not form, while the lower grouping is composed of experiments in which formation occurred. Thus, in the experiments for which a recirculating bulge formed, the coastal current is shorter in extent (with correspondingly smaller velocities) and narrower in width, at any given point in the flow's evolution.

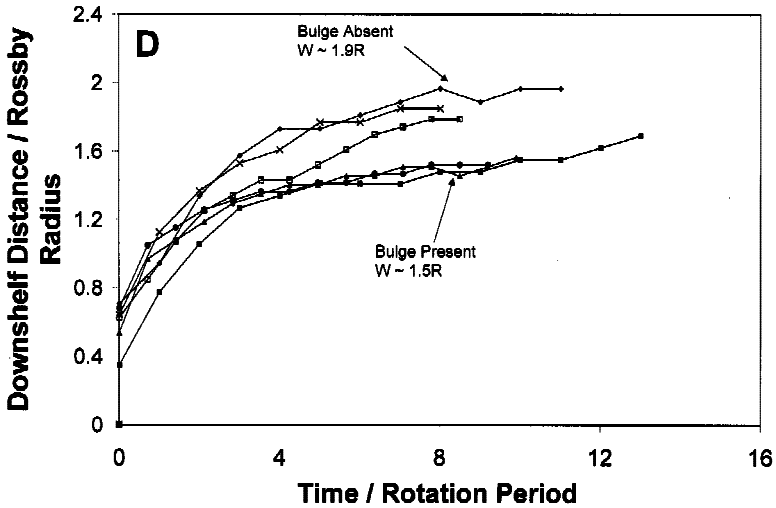
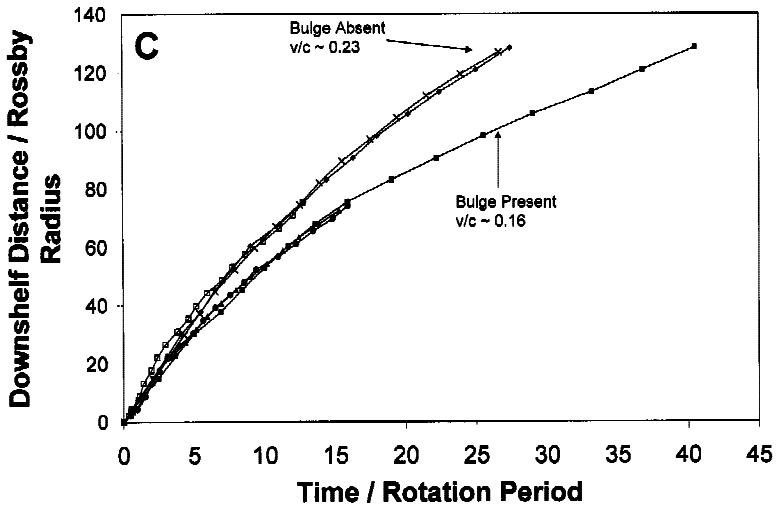


Figure 4. (Continued)

recirculating bulge on the coastal current is the same, independent of the specific characteristics of the bay exit region.

The coastal current can be approximated as a linearly stratified wedge. Previous laboratory studies (e.g. Avicola and Huq, 2002) as well as field data of coastal currents under low wind conditions (e.g. Münchow and Garvine, 1993a) demonstrate that this is a reasonable approximation. A simple analytical estimate for the density anomaly flux and volume flux through the coastal current cross-section can then be obtained. The density surfaces of a linearly stratified wedge can be described as:

$$\Delta\rho(y, z) = \Delta\rho_0 - \Delta\rho\left(1 - \frac{z}{D} - \frac{y}{W}\right) \quad (5)$$

where D and W represent the maximum depth and width of the wedge of the buoyant fluid. Thermal wind balance requires the velocity structure within the wedge to vary as:

$$v(y, z) = v_s(0) - \frac{g}{\rho f} \int \frac{\partial\rho}{\partial y} dz. \quad (6)$$

Eq. 6 can be rewritten as:

$$v(y, z) = v_s(0) - \frac{g}{\rho f} \frac{\Delta\rho}{W} z. \quad (7)$$

Because we require the lower (ambient ocean) layer to be quiescent, the velocity must be zero at the edge of the wedge of the buoyant fluid. Applying this boundary condition yields:

$$v(y, z) = \frac{g}{\rho f} \frac{\Delta\rho}{W} \left[\left(D - \frac{y}{W} D \right) - z \right]. \quad (8)$$

The maximum velocity occurs at $y = 0, z = 0$: we define V to be the maximum velocity of the wedge, such that:

$$V = \frac{g'D}{fW}. \quad (9)$$

Thus, the functional form of the velocity is simply:

$$v(y, z) = V \left(1 - \frac{y}{W} - \frac{z}{D} \right). \quad (10)$$

From Eqs. 5 and 10, the volume and density anomaly fluxes can be calculated. Solving the integrals results in the following estimates for the coastal current volume flux and the coastal current density anomaly flux:

$$Q_{cc} = \frac{1}{6} WDV \quad (11)$$

$$M_{cc} = \frac{1}{12} WDV\Delta\rho. \quad (12)$$

Estimates of plume width and depth are determined from Figures 3 and 4. Measurements of mean maximum velocity in the coastal current were also determined. These measurements were taken at a distance of $20R$ downstream from the source at times between 12 to 16 rotation periods from the start of the experiments. Using these data, we estimate the

Table 2. Volume flux and density anomaly flux values for the coastal currents which formed in each of the experiments in this study are tabulated. The source volume flux and density anomaly flux are known. Experimental data were used to estimate the coastal current volume and density anomaly flux values based upon maximum velocity, coastal current width, and coastal current depth. Width was measured visually in all experiments. Based upon density cross-sections, the maximum depth was estimated based upon width information. The ratio of coastal current transport to source transport of volume and density anomaly are listed in the right-hand columns. Values of the estimated coastal current volume flux are larger than the source volume flux due to mixing near the source.

Name	Q_0	$\Delta\rho$	M_0	$V(\max)$	W	h	Q_{cc}	M_{cc}	Q_{cc}/Q_0	M_{cc}/M_0
units	cm ³ /s	g/cm ³	g/s	cm/s	cm	cm	cm ³ /s	g/s	—	—
RB1	9.5	0.015	0.138	2.3	8.8	2.2	7.5	0.055	0.79	0.40
RB2	10.0	0.005	0.050	1.9	5.3	4.5	7.4	0.019	0.74	0.37
RB3	10.0	0.006	0.055	1.8	5.5	4.6	7.4	0.020	0.74	0.37
RB4	10.0	0.016	0.160	2.4	9.2	2.1	8.0	0.064	0.80	0.40
CC1	10.0	0.014	0.140	3.1	12.3	2.9	18.6	0.130	1.86	0.93
CC2	10.0	0.006	0.055	2.4	7.3	5.8	16.8	0.046	1.68	0.84
CC3	10.8	0.006	0.065	2.3	7.2	6.0	16.8	0.050	1.55	0.78
CC4	10.0	0.015	0.150	3.3	12.2	3.0	20.2	0.151	2.01	1.01
CC5	10.0	0.005	0.050	2.4	7.2	6.1	17.5	0.044	1.75	0.87
CC6	10.0	0.005	0.053	2.5	7.2	6.0	18.0	0.047	1.80	0.90
CC7	10.0	0.015	0.145	3.3	12.1	3.0	20.0	0.145	1.99	1.00
CC8	10.0	0.006	0.055	2.4	7.2	6.1	17.2	0.047	1.72	0.86
CC9	10.0	0.015	0.150	3.1	12.2	3.0	18.8	0.141	1.88	0.94

volume and density anomaly flux in each coastal current from Eqs. 11 and 12. These data are tabulated in Table 2.

Data presented in Table 2 are delineated in the same manner as in Table 1: experiments for which a recirculating bulge was observed to form are shaded light gray. In the last two columns of the table, ratios between the coastal current estimates and the source values of volume flux and density anomaly flux are shown. For the experiments in which no recirculating bulge formed, the estimate of the density anomaly flux in the coastal current is 90% of the density anomaly flux input at the source. Thus, the density anomaly flux output at the source is nearly equal to that measured downstream from the source. Although the small amount of missing density anomaly is within experimental error, it may be due to the small amount of flux contributing to offshore growth of the coastal current. Also shown are the estimates of the volume flux: for the experiments in which recirculating bulges did not form, the estimated coastal current flux was approximately 1.8 times that of the source volume flux. The fact that the volume flux estimate in the coastal current is double the source volume flux is consistent, as examination of Eqs. 11 and 12 shows that when the density anomaly flux in the coastal current is equal to the source density anomaly flux, the volume flux must be double that for a coastal current approximated as a stratified wedge.

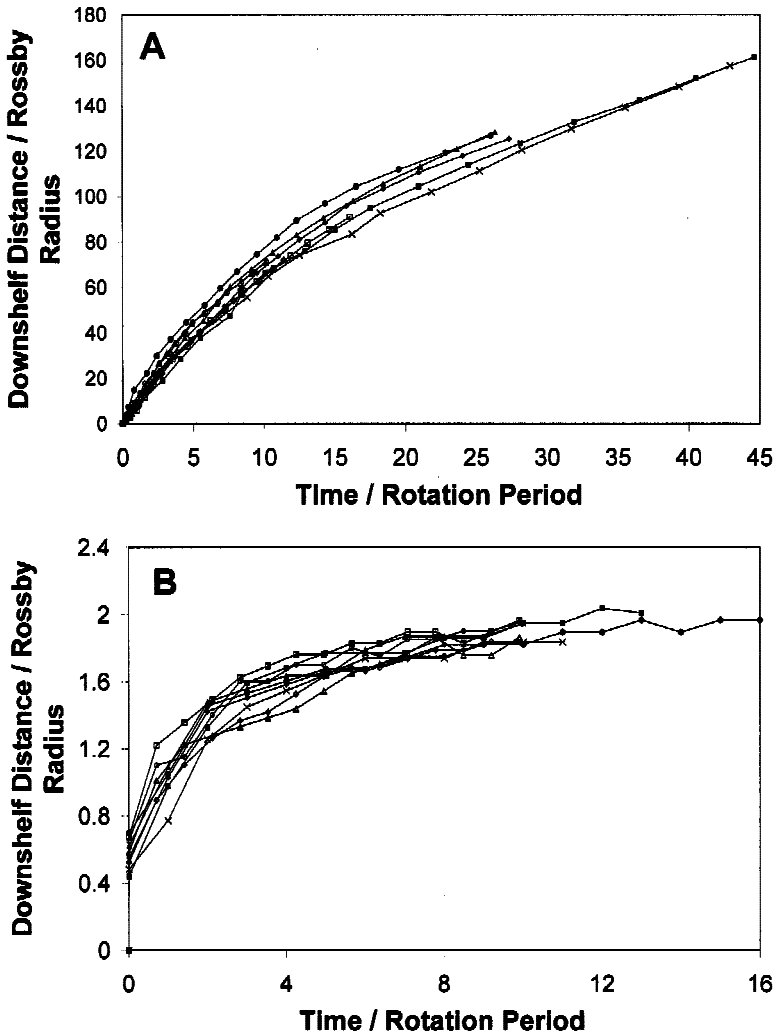


Figure 5. Graphs of coastal current evolution data as a function of time. These figures are plotted in the same manner and the same order as in Figure 3. However, in this figure, the internal Rossby radius, R , is re-scaled for experiments in which a recirculating bulge formed; this rescaling was used to take into account the reduced flow rate fed to the coastal current from the recirculating bulge. The affected experiments have been rescaled such that 40% of the source volume flux was used to produce the scale R^* . This estimate indicates that, in experiments in which a recirculating bulge forms, $\sim 60\%$ of the source volume flux is absorbed into the recirculating bulge region, while the remaining $\sim 40\%$ is transported in the coastal current. The effect of rescaling the flow rate is to collapse the data of the coastal current evolution.

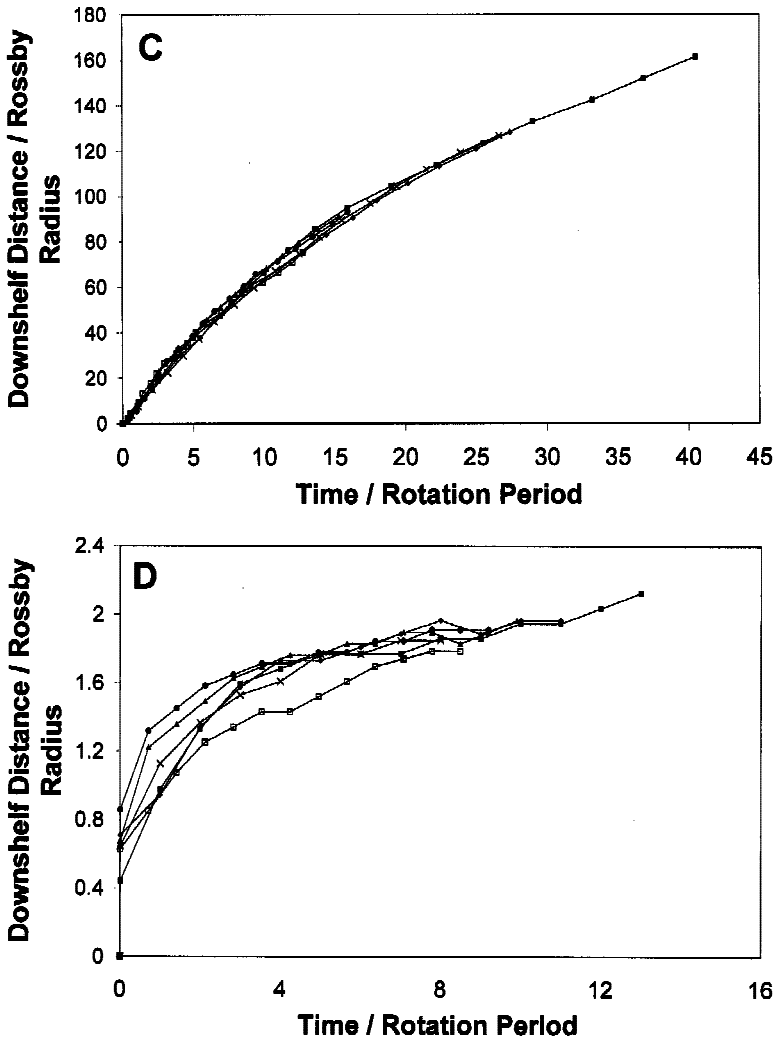


Figure 5. (Continued)

This indicates that mixing has occurred in the out flow: observations suggest this mixing occurs very close to the source (within a few Rossby radii).

In contrast, experiments in which a recirculating bulge was observed to form have considerably less transport in their coastal currents. For these experiments, approximately 40% of the source density anomaly flux is observed to be present in the coastal current. Similarly, only 80% of the source volume flux is observed within the coastal current (as opposed to 1.8 times that of the source volume flux for bulge-less coastal currents). Visual observations show that there is no significant transport upshelf or offshore from the source region: thus the mixing transport must be stored in the recirculating bulge. These

measurements demonstrate that for the experiments in which a recirculating bulge was observed to form, between 40%–50% of the source density anomaly σ_θ is being transported in the coastal current, with the remaining 60%–50% being stored in the growing bulge region.

plotted in Figure 4 showed two distinct groups; the rescaling used in Figure 5 collapses the data. All of the experiments now evolve in the same manner, within a narrow envelope. Thus, using an independent measurement technique from that of the volume flux calculations of Section 3a, a comparable estimate was found: ~40% of the source volume flux was observed to be transported downshelf within the coastal current. Furthermore, the collapse of the data is good for all times, which suggests that the volume flux fed to the coastal current is constant. If the value of χ was a function of time, the use of a constant percentage (40%) of the source volume flux into the coastal current would not adequately collapse the data.

The data from these experiments indicate that the percentage of buoyant fluid stored within the recirculating bulge (when it forms) is approximately 60% of the source mass flux and relatively constant with time. This observation has also been made in other studies, including Fong, 1998 (numerical study) and Nof and Pichevin, 2001 (numerical/analytical study), but the dynamical reasons for these percentages are not yet understood.

4. Evolution of the recirculating bulge

Examination of the impact of a recirculating bulge on coastal current transport establishes that approximately 60% of the source volume flux and density anomaly flux are stored in the bulge region. Turning to the bulge region itself, it is possible to examine its evolution directly. (The overall dimensions of the recirculating bulge were shown previously in Figure 3.) Figure 6 is a set of graphs in which the recirculating bulge length (Panel A), width (Panel B), depth (Panel C), and estimated volume (Panel D) are plotted logarithmically. As before, distance has been nondimensionalized by the scale internal Rossby radius, R , and time by the rotation period, T . Volume measurements have been nondimensionalized by the source daily volume, $Q_0 T$. The form of the temporal evolution of the bulge growth can be determined by plotting the data nondimensionally in this manner. Best-fit estimates of growth rate have been fitted to the data plotted in Figure 6 and are shown as the solid lines.

Both the bulge length (Panel A) and width (Panel B) are observed to grow at the same rate, with a best-fit estimate of $r \propto t^{2/5}$. Similarly, recirculating bulge depth measurements are plotted in Figure 6C. It is evident that the recirculating bulge depth's growth is less dramatic than that of the horizontal dimensions. The depth doubles in the course of the experiment (~20 rotation periods) while the horizontal scales increase by an order of magnitude in the horizontal scales over the same time frame. The depth evolution is found to follow a best-fit estimate of $H \propto t^{1/5}$.

It is possible to calculate the recirculating bulge volume as a function of time from estimates of the horizontal and vertical scales. This calculation is plotted in Figure 6D. The volume estimate shown is based upon the simple formula:

$$V_B = k\pi \frac{W L}{2} D \tag{16}$$

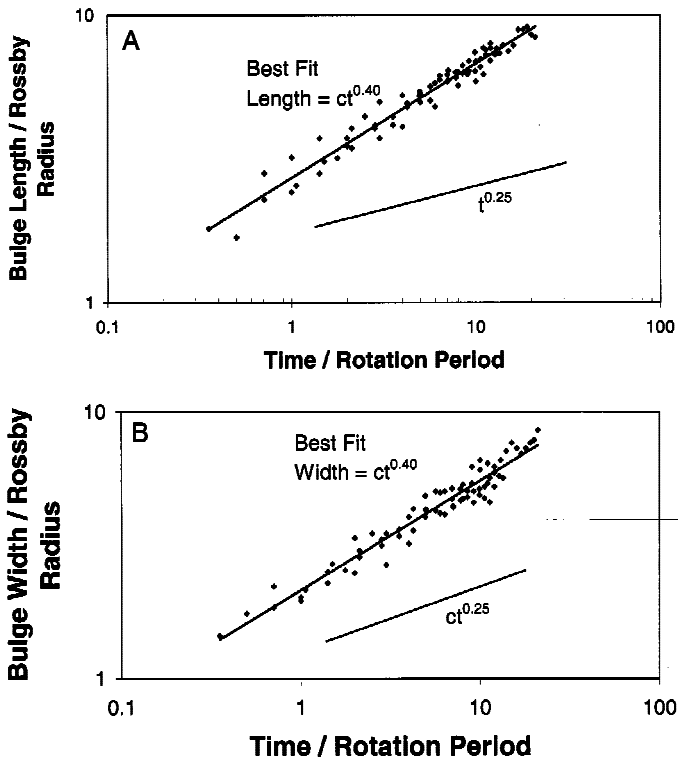


Figure 6. Graphs in which the dimensions of the recirculating bulge are plotted as a function of time. Data are plotted in nondimensional form, scaled by the Rossby radius, R , the source volume (QT), and the rotation period, T . The data are plotted in log-log form, from all experiments in which a recirculating bulge was observed to form. Also plotted is a best- t power estimate for the growth rate of each quantity. Panel A is a plot of the maximum recirculating bulge length (along-shore extent), Panel B is a plot of maximum recirculating bulge width (across-shore extent), Panel C is a plot of the maximum recirculating bulge depth, and Panel D is a plot of the estimated recirculating bulge volume. From the data presented in this figure, it can be seen that the horizontal scales of the bulge (length and width) grow as $\sim t^{2/5}$ power, the depth scale grows as $\sim t^{1/5}$ power, and the volume grows approximately linearly with time. Also shown are lines which represent a $t^{1/4}$ growth rate (Panels A and B) and a $t^{1/2}$ growth rate (Panel C).

where k is the shape constant of the radial depth profile. As this shape constant of the recirculating bulge is not known, it was set equal to unity for the estimates shown in Figure 6D. From Figure 6D it can be seen that the bulge volume grows approximately linearly with time. This was expected as the estimate of the transport constant, χ , used to produce Figure 5 was a constant 40% and collapsed the data well over the entire duration of the experiment. Other studies have also found that the bulge volume grows linearly with time, including Fong (1998) and Nof and Pichevin (2001).

The time evolution of the bulge's horizontal and vertical scales, seen in Figure 6, differs

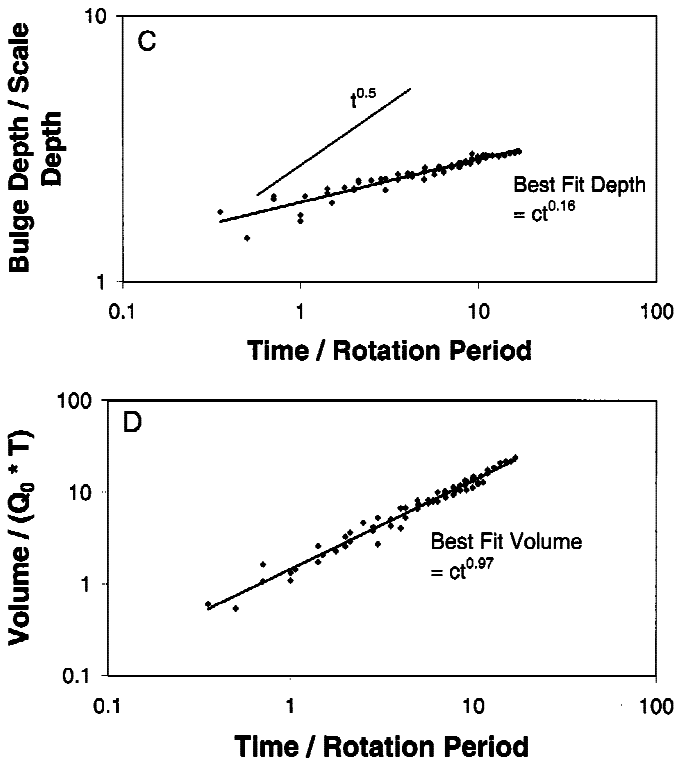


Figure 6. (Continued)

from that of an elliptical buoyant lens in thermal wind balance. Thermal wind balance requires:

$$fv = g' \frac{\partial Z}{\partial y} \tag{17}$$

where v is the radial velocity of the recirculating bulge, and $\partial Z/\partial y$ is the isopycnal slope of the recirculating bulge. If the scale velocity (Eq. 4) and scale isopycnal slope are substituted into Eq. 17, the following scaling emerges:

$$f\sqrt{g'_0 H} \approx g'_0 \frac{H}{r} \tag{18}$$

where H and r represent the bulge maximum depth and radius respectively. Eq. 18 can be rewritten as:

$$H \approx \frac{f^2 r^2}{g'_0} \tag{19}$$

The volume of the recirculating bulge can be written as:

$$V_b \approx k\pi r^2 H. \quad (20)$$

Combining Eqs. 19 and 20 results in an expression for the volume of the recirculating bulge:

$$V_b \approx \frac{k\pi f^2 r^4}{g'_0}. \quad (21)$$

As before, k is an unknown constant of order one that is dependent upon the radial depth profile of the recirculating bulge. If the assumption is made that the volume flux added to the bulge ($Q_0 = (1 - \chi)Q_b$) is constant with time, then Eq. 21 can be rewritten as:

$$Q_{bt} = V \approx \frac{k\pi f^2}{g'_0} r^4. \quad (22)$$

Therefore, the growth rates of the radius and maximum depth of the recirculating bulge can be estimated as:

$$r \approx \left(\frac{g'_0 Q_{bt}}{k\pi f^2} \right)^{1/4} \quad (23)$$

$$H \approx \left(\frac{f^2 Q_{bt}}{k\pi g'_0} \right)^{1/2}. \quad (24)$$

The estimated growth rates shown in Eqs. 23 and 24 predict time dependent growth rates of $r \propto t^{1/4}$ and $H \propto t^{1/2}$. Note that these growth rates are markedly different from the observed growth rates of $r \propto t^{2/5}$ and $H \propto t^{1/5}$ of the experiments (as seen in Fig. 6).

The thermal wind growth rates of Eqs. 23 and 24 have also been predicted and examined in a number of previous studies. Griffiths and Linden (1981) examined baroclinic vortices, including experiments in which a constant volume flux source was used to form the vortex. Such vortices are similar in structure to the recirculating bulge regions formed in these experiments, with the exception of the coastal wall present in the current study. Using potential vorticity and the geostrophic assumption, they predicted growth rates of $r \propto t^{1/4}$ and $H \propto t^{1/2}$ for their experiments. For experiments conducted by Griffiths and Linden, the measured geostrophic growth rates were in accord with Eqs. 23 and 24. Note, however, that this growth rate was observed only during the initial phase of the evolution of the baroclinic vortex. For long times, they observed that the baroclinic vortex would become unstable, resulting in large horizontal growth and a thinning in the vertical.

Nof and Pichevin (2001) examined bulge formation from the standpoint of momentum conservation. They assumed that the bulge volume flux, Q_b , would be constant with time, based upon their numerical/theoretical configuration. Their analysis predicts that the recirculating bulge should grow as:

$$r = \left(r_i^4 + \frac{32g'Q(t-t_i)}{\pi f^2(1+2\alpha)(2-\alpha)} \right)^{1/4} \quad (25)$$

$$H = \left(H_i^2 + \frac{f^2\alpha^2(2-\alpha)Q(t-t_i)}{(1+2\alpha)2\pi g'} \right)^{1/2} \quad (26)$$

where α denotes the potential vorticity (PV) of the outflow ($\alpha = 1$ reduces to the zero PV case). Note that the functional form of Eqs. 23 and 24 are identical to 25 and 26, for any time-independent value of PV . However, there is a difference between Nof and Pichevin's analytical predictions given by Eqs. 25 and 26, and the data from their numerical simulations. Results from their numerical simulations for horizontal growth (Fig. 7 of their paper) and vertical growth (Fig. 8 of their paper) demonstrate that their numerical model predicts much greater horizontal growth and weaker vertical growth than those given by Eqs. 25 and 26. They propose that friction slows the rotation of their bulge region and alters the potential vorticity with time (PV is not constant), and thus changes the temporal growth rate of the bulge.

Fong (1998) estimated that for his numerical experiments, the radial extent of the recirculating bulge grew approximately like the square root of time (Fig. 2.15 of his dissertation). This value is reasonably close to the observed $t^{2/5}$ power seen in this study.

Klinger's (1994b) laboratory study results are an interesting comparison with those of the current study. His experiments have some differences in experimental setup worthy of note: the outflow was generated by a dam break, rather than a continually pumped outflow, and his 'bay exit' was a large Kelvin number exit, rather than the $K = 1$ used in these experiments. For experiments with a 90-degree corner angle, his results (Klinger's Fig. 7) show a recirculating bulge which grows with time in a similar fashion as in this study, until the bulge separates from the wall (which occurs between 8 and 12 rotation periods). He noted that this separation did not appear when the experiment was performed with a continually pumped outflow, and speculated that this separation was caused by the lower layer return outflow (due to the dam break source condition). Klinger's (1994b) experiments based upon a 45-degree corner angle also showed eddy formation: this is in contrast with the experiments conducted in this study. This is discussed further in the companion paper, Avicola and Huq (2003).

Therefore, the question becomes, what is the mechanism which forces the recirculating bulge region to grow in the manner in which it is observed (large horizontal growth $R \propto t^{2/5}$, small vertical growth $H \propto t^{1/5}$), rather than the prediction of Eqs. 23 and 24? For the recirculating bulges observed in these experiments, instabilities were observed to be present for nearly the entire duration of the experiment. Saunders (1973) examined instability in baroclinic vortices. He described the wavenumber of the instability of the baroclinic vortex as follows: $n = 0$ describes a stable vortex, $n = 1$ describes a vortex with a single core but asymmetric form, $n = 2$ and larger indicate multiple cores. The multiple cores are each a vortex (with associated rotation), which are also rotating (precessing)

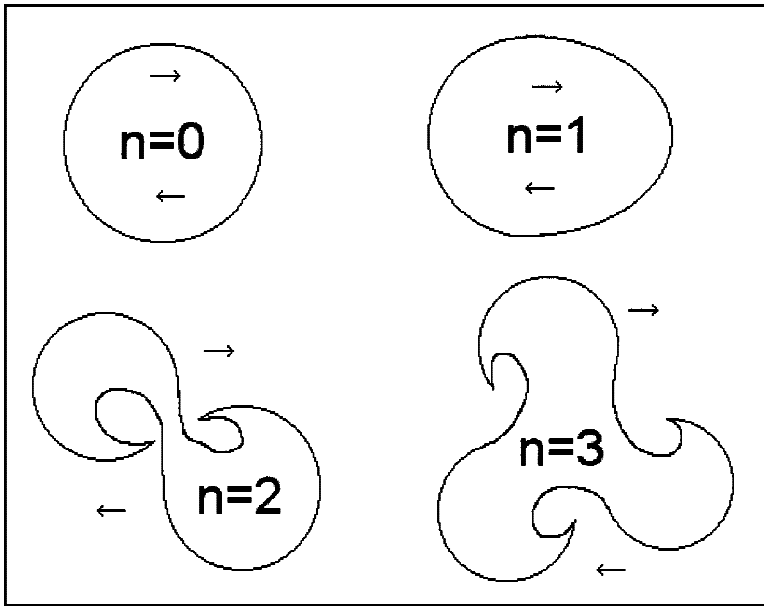


Figure 7. Schematic in which representations of baroclinic vortex instabilities are portrayed for four wavenumbers. Such phenomena are described in Griffiths and Linden (1981). A value of zero for the wavenumber, n , indicates a stable baroclinic vortex. Such a vortex is circular in cross-section. A wavenumber of one is indicative of a bar-like instability, in which the vortex is no longer circular. Rather, it is elliptical or irregular, with uneven rotation. For a vortex with a constant volume flux, the bulge will precess with the same sign of rotation as the fluid within the vortex. For a wavenumber of 2, the vortex is split into two distinct cores, each comprising a cyclone and an anticyclone. For the observed experiments, the high (anticyclone) of the pair was a much stronger feature, while the low (cyclone) quickly disappeared. The two cores rotate about the center of rotation. Higher wavenumbers indicate a larger number of cores.

about the center of the baroclinic region. Figure 7 describes this instability mechanism schematically.

This description is an accurate portrayal of the recirculating bulge features seen in this study, some photographic examples of which are shown in Figure 8. Figure 8 shows three images taken of experiment RB1. The upper image was taken at $t = 1T$, the middle at $t = 5T$, and the lower at $t = 10T$. Note that in all three images in Figure 8, there is an outer 'halo.' This region is a thin, surface layer of dye. Measurements of the recirculating bulge's dimensions were taken from video observations of the velocity field, this outer 'halo' was characterized by extremely small velocities, and was not included in these measurements.

Also shown in Figure 8 are markings indicating the anticyclonic cores of the bulge. Note that the upper panel ($t = 1T$) shows a recirculating bulge that consists of one core, elliptical in shape: thus, this represents a bulge region with a wavenumber of 1. This core has been marked as 'A'. The middle panel ($t = 5T$) shows that the recirculating bulge has

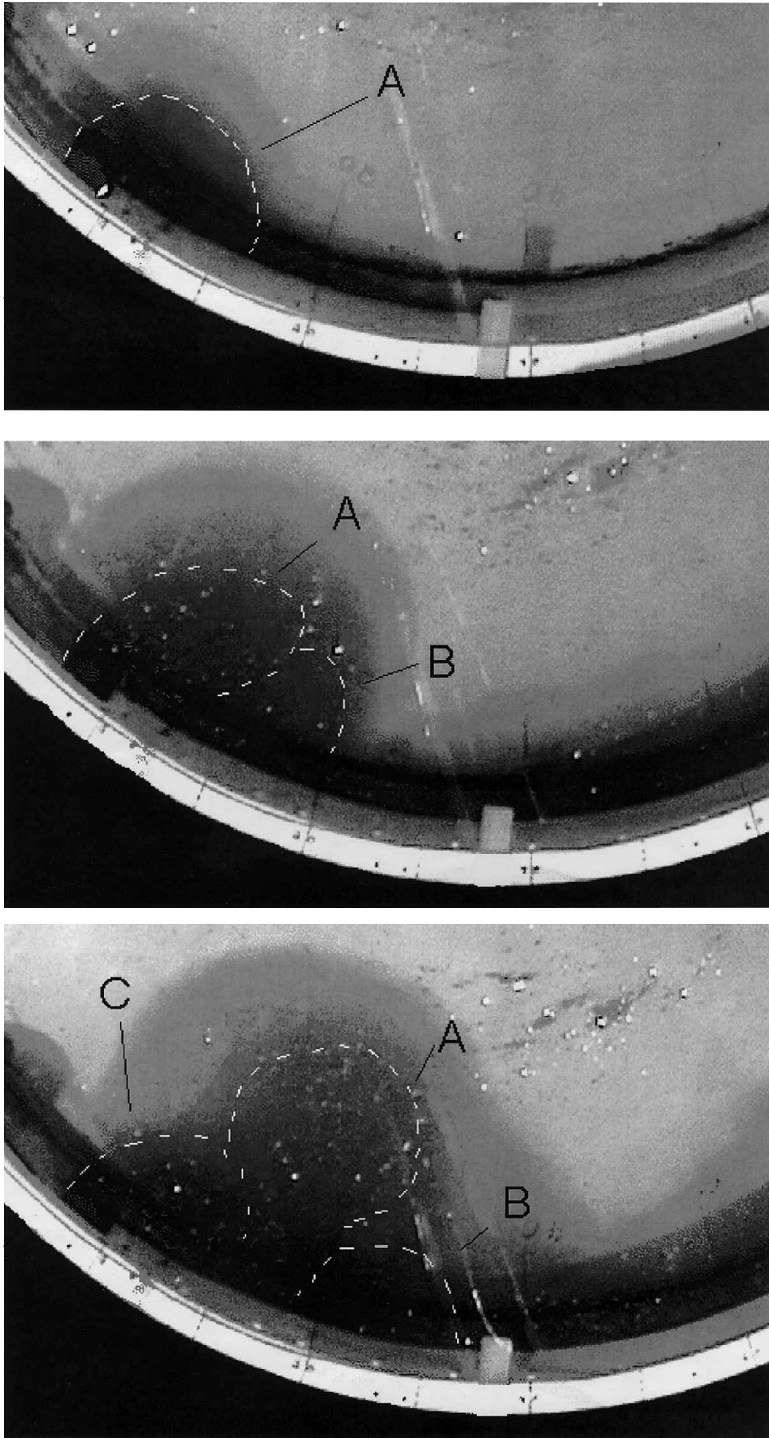


Figure 8. Images captured from the video records of a realization of experiment RB1. The images were taken (from top to bottom) at $t = 1T$, $5T$, and $10T$ from the start of the experiment. Markings in the images indicate the extent of the anticyclonic circulation regions observed in the bulge.

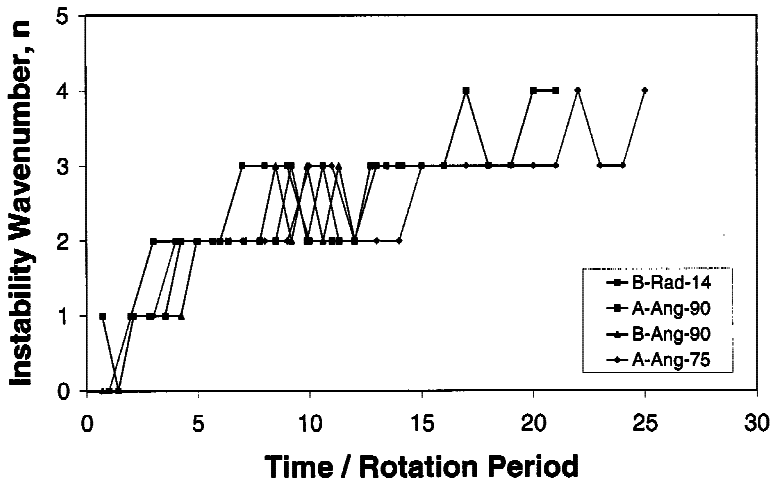


Figure 9. Plot of the observed wavenumber of the recirculating bulge instabilities as a function of time for experiments in which a recirculating bulge was observed to form. For each experiment, the visual record was examined at numerous times, and the wavenumber of the bulge instability was ascertained. This process was relatively subjective, as the recirculating bulge is interacting with the coastal wall, and thus, the instabilities of the bulge region are generally not well behaved. Thus, as shown in this figure, the estimated wavenumber of the bulge often oscillates between two values (for example, between 7 and 15 days, the wavenumber oscillates between $n = 2$ and $n = 3$). However, a clear trend of increasing wavenumber as the recirculating bulge evolves. It is also clear that the recirculating bulge is never stable, as the bulge was observed to transition into mode one immediately after the flow impacted the coastal wall and circulation developed.

grown. At this time, the image is interpreted as a recirculating bulge with a single elliptical core 'A' adjacent to the bay exit, and a smaller core downshelf of the first core and trapped against the wall, 'B' ($n = 2$). The recirculating bulge transitions from the $n = 1$ to the $n = 2$ state at a time near $t = 5T$: the state shown in the middle panel of Figure 8. Thus, core 'A' in the upper panel has evolved into a state in which it has broken into two cores, 'A' and 'B', in the second panel. Finally, the third panel of the recirculating bulge ($t = 10T$) shows three cores. Cores 'A' and 'B' are present from the earlier panel (having precessed around the common center), such that core 'A' is now detached from the wall, and core 'B' is now sandwiched between 'A' and the coastal wall. The video records show that core 'B' is waning, and is seen to disintegrate against the coastal wall near this time. Core 'C' is a new anticyclonic core that has begun to form (and grow in size) at the mouth of the estuary: this core began to form as 'A' rotated away from the mouth.

The wavenumber of the instability was measured at numerous times for each experiment, based upon visual observations of the flow. As seen from Figure 8, this is a subjective exercise, complicated by the fact that the unstable baroclinic vortex is interacting with a coastal wall. Consequently, values of the wavenumber of the observed instability tend to jump between states. The wavenumber evolution is plotted in Figure 9:

the estimated wavenumber, n , is shown as a function of time for the experiments in which a recirculating bulge was observed to form. While there is a large amount of noise, as the wavenumber oscillates between two values, there is a clear trend of the instability wavenumber increasing with time over the course of the experiments. The oscillations between wavenumber (for example, between 7 and 15 days the experiments oscillate between $n = 2$ and $n = 3$) are largely due to the interactions of the instabilities with the wall.

The first visual sign of $n = 1$ and $n = 2$ instabilities were seen between days 2 and 3 for each experiment. The formation of the recirculating bulge occurs at approximately one day after the outflow exits the bay (see Fig. 2). Thus, the recirculating bulge region appears to be unstable from its inception. Saunders (1973) determined experimentally that a baroclinic lens may be unstable, as governed by the dimensionless instability parameter,

$$\Theta = \frac{g'H}{r^2f^2} = \frac{\tilde{H}}{\tilde{r}^2}. \tag{27}$$

Its inverse will be used in this study:

$$I = \frac{r^2f^2}{g'H} = \frac{\tilde{r}^2}{\tilde{H}} \tag{28}$$

where the dimensionless quantities \tilde{H} and \tilde{r} , are simply the dimensionless maximum bulge depth H/h and bulge radius r/R , respectively. The instability parameter, I , is a ratio of the Coriolis force due to the recirculating fluid to the baroclinic buoyancy force due to the isopycnal slope. Alternatively, it can be seen to be a ratio of the rotational kinetic energy to the available potential energy in a baroclinic vortex. Values of the instability parameter, I , greater than one indicate that instabilities may form with larger values corresponding to larger values of the wavenumber, n .

The experiments of Saunders (1973) were constant volume (instantaneous release) experiments; therefore, his definitions of H and r in Eq. 27 are the initial depth and radius of the cylinder of buoyant fluid before release. However, the present study is a constant volume flux experiment. Therefore, the definition of I (Eq. 28) will utilize time-varying quantities: H = measured maximum bulge depth, r = measured maximum bulge radius. Using the values measured for each experiment (as seen in Fig. 3) an estimate for the instability parameter, I , can be obtained. Figure 10 is a plot in which values of the instability parameter as a function of time are shown. Values of the instability parameter, I , range from 1.1 to 20 over a period of approximately 20 experimental days: the recirculating bulge begins at a slightly unstable state and evolves with time to larger values of the instability parameter. The time evolution of the instability parameter grows as approximately $I \propto t^{3/5}$.

Figure 11 plots the observed instability wavenumber, n , for each experiment as a function of the instability parameter, I , estimated at the time of the observation. As an experiment evolves, values of both the wavenumber and instability parameter increase

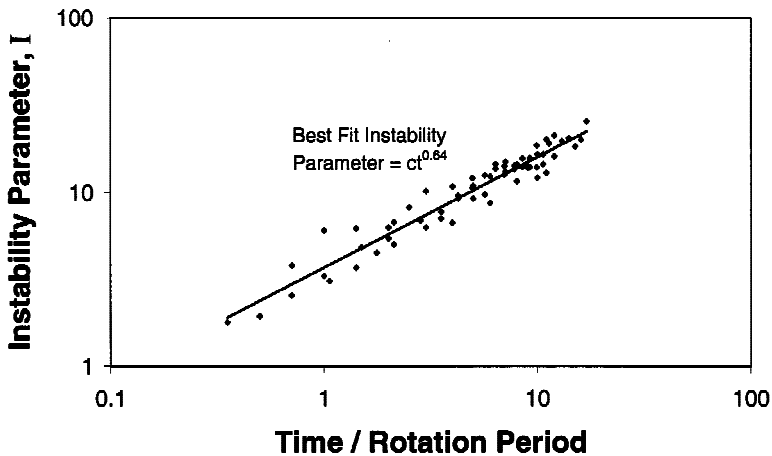


Figure 10. Graph of the instability parameter, I , as a function of time. Values of the instability parameter are plotted for all experiments in which a recirculating bulge was observed to form. The instability parameter is the inverse of the parameter shown in Saunders (1973) and is a ratio of the Coriolis force to the buoyancy force, or alternatively, a ratio of the rotational kinetic energy to the available potential energy of a baroclinic vortex. Values larger than one indicate that the bulge region should become unstable, with larger values of the instability parameter indicating higher wavenumber instabilities in the baroclinic vortex. In this figure, the instability parameter, I , is estimated based upon the maximum bulge width and depth measurements which were plotted in Figure 5. Note that the measured values of the instability parameter are always greater than one, and increase in magnitude with time. A best-fit power estimate has been fitted to the data.

with time. Therefore, the experiments begin at the lower left and evolve with time toward the upper right (as indicated by the arrow). The data in this figure show a trend of increasing instability wavenumber with increasing values of the instability parameter. Also plotted are the maximum and minimum values of each wavenumber as seen in Saunders (1973). The experimental data evolve in the same manner as the Saunders' data but with an offset. This is most likely due to the differences between the definitions of the instability parameter between constant-release and constant-flux experiments.

Thus, this observed instability mechanism is a possible explanation for the discrepancy between the observed growth rates $H \propto t^{1/5}$, $r \propto t^{2/5}$; and the geostrophic growth rates $h \propto t^{1/2}$, $r \propto t^{1/4}$. The growth characteristics of the unstable bulge are in accord with numerical studies of recirculating bulge phenomena, which also produce bulges with rapidly growing horizontal scales combined with weak vertical growth (Fong, 1998; Nof and Pichevin, 2001). The 90-degree exit angle experiments of Klinger (1994b) did not show instabilities of order $n = 2$ or higher; however, as previously stated, the bulge in this experiment was observed to detach from the coastal current flow after ~ 8 rotation periods. Thus, the bulge of Klinger (1994b) may not have had sufficient time to generate higher wavenumber instabilities. Instabilities of the type seen in Saunders (1973), Griffiths and Linden (1981), and this study, have not been reported in the numerical models. It is likely that instabilities

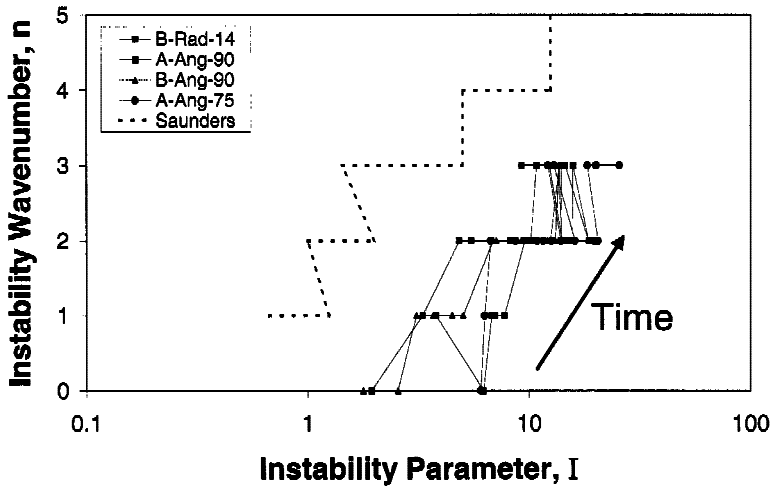


Figure 11. Graph in which the observed instability wavenumber, n , is plotted as a function of the instability parameter, I , for the experiments in which a recirculating bulge was observed to form. The instability wavenumber for each experiment (seen in Fig. 10) was plotted against the value of the instability parameter (Fig. 11) for each measurement. The resulting graph shows the evolution of the instability wavenumber for the recirculating bulge region as a function of the instability parameter. Larger values of both the instability wavenumber and the instability parameter occur as the experiment evolves in time. Therefore, the temporal evolution of the data in this plot is towards the upper right, as indicated by the arrow. The results from the experiments of Saunders (1973—his Fig. 3), are plotted in comparison to our experiments.

within the bulge region may have some dependence upon the vorticity distribution of the buoyant outflow, both in numerical and laboratory studies, and such distributions are likely to vary between numerical models, laboratory experiments, and source conditions (e.g. dam break vs. pump source). The mechanism of instability formation in the recirculating bulge region certainly deserves more attention in future studies.

5. Summary and conclusions

Laboratory experiments were conducted which examined the growth and characteristics of a recirculating bulge region formed from a surface advected plume exiting a strait or estuary. Conducted experiments included samples with and without bulge formation. It was found that in experiments for which recirculating bulge formation occurred, the coastal current scales were attenuated: the coastal current width, length, and velocities were significantly reduced.

Measurements of the volume (and buoyancy) storage within the recirculating bulge were undertaken. Flux measurements indicated that for experiments with a recirculating bulge, approximately 40% of the source volume flux was transported downshelf in the coastal current: this flow rate reduction accounts for the reduced scales of the coastal current for

such experiments. A second method of determining the bulge volume storage was obtained by re-estimating the scales of the coastal current discharge for the experiments in which a recirculating bulge was formed. The coastal current u_x estimate obtained from this re-scaling was also 40% of the source volume u_x . The use of this reduced source volume u_x collapses the data for the geometrical scales of the coastal currents.

The growth rates of the recirculating bulge scales were also calculated. The horizontal scales of the bulge region were found to grow quickly with time ($R \propto t^{2/5}$). However, the vertical scales of the recirculating bulge grew relatively slowly ($h \propto t^{1/5}$). In addition, a stable geostrophic lens with a constant (

- coastal current transport, 5th International Symposium on Stratified Flows, International Association of Hydraulic Research, Vancouver, Canada, 865–870.
- Jiang, X. 1995. Flow separation by interfacial upwelling in the coastal ocean, M.S. thesis, University of Victoria, 64 pp.
- Kawasaki, Y. and T. Sugimoto. 1984. Experimental studies on the formation and degeneration processes of the Tsugaru warm gyre, *in* Ocean Hydrodynamics of the Japan and East China Sea, T. Ichiye, ed., D. Reidel Publishing Company, 225–238.
- Klinger, B. A. 1994a. Inviscid current separation from rounded capes. *J. Phys. Oceanogr.*, *24*, 1805–1811.
- 1994b. Baroclinic eddy generation at a sharp corner in a rotating system. *J. Geophys. Res.*, *99(C6)*, 12515–12531.
- Lanoix, F. 1974. Project Alboran: Hydrologic and dynamic study of the Alboran Sea (in French), Tech rep. 66, N. Atl. Treaty Org., Brussels.
- Münchow, A. and R. W. Garvine. 1993a. Buoyancy and wind forcing of a coastal current. *J. Mar. Res.*, *51*, 293–322.
- 1993b. Dynamical properties of a buoyancy-driven coastal current. *J. Geophys. Res.*, *98(C11)*, 20063–20077.
- Nof, D. and T. Pichevin. 2001. The ballooning of outflows. *J. Phys. Oceanogr.*, *31*, 3045–3058.
- Oey, L.-Y. and G. L. Mellor. 1993. Subtidal variability of estuarine outflow, plume, and coastal current: A model study. *J. Phys. Oceanogr.*, *23*, 164–171.
- Pichevin, T. and D. Nof. 1997. The momentum imbalance paradox. *Tellus*, *48A*, 298–319.
- Saunders, P. M. 1973. The instability of a baroclinic vortex. *J. Phys. Oceanogr.*, *3*, 61–65.
- Savage, S. B. and R. J. Sobey. 1975. Horizontal momentum jets in rotating basins. *J. Fluid Mech.*, *71*, 755–768.
- Simpson, J. H., W. G. Bos, F. Schirmer, A. J. Souza, T. P. Rippeth, S. E. Jones and D. Hydes. 1993. Periodic stratification in the Rhine ROFI in the North Sea. *Oceanol. Acta*, *16*, 23–32.
- Smeed, D. A. 1988. Baroclinic instability of three-layer flows—Part 2. Experiments with eddies. *J. Fluid Mech.*, *194*, 233–259.
- Whitehead, J. A. 1985. The deflection of a baroclinic jet by a wall in a rotating fluid. *J. Fluid Mech.*, *157*, 79–93.
- Whitehead, J. A. and A. R. Miller. 1979. Laboratory simulation of the gyre in the Alboran Sea. *J. Geophys. Res.*, *84(C7)*, 3733–3742.
- Yankovsky, A. E. and D. C. Chapman. 1997. A simple theory for the fate of buoyant coastal discharges. *J. Phys. Oceanogr.*, *27*, 1386–1401.

Received: 10 March, 2003; revised: 27 May, 2003.